Soft Matter

ARTICLE TYPE

Cite this: DOI: 10.1039/xxxxxxxxxx

# Chemical Leslie Effect in Langmuir Monolayers: a complete experimental characterization†

Félix Bunel,*[a,b] Jordi Ignés-Mullol,[b,c] Francesc Sagués[b,c] and Patrick Oswald[a]

Received Date
Accepted Date

DOI: 10.1039/xxxxxxxxxx

www.rsc.org/journalname

We propose a complete characterization of the chemical Leslie effect in a Langmuir monolayer of a chiral liquid crystal. In this goal, we developed new experimental techniques using an electric field and an humidifier to prepare large monodomains in which the molecules can freely rotate. We also designed six independent experiments to precisely measure the four material constants involved in the dynamics of the monolayer, namely the Leslie coefficient, the rotational viscosity, the curvature elasticity constant and the surface polarization. The relevance of the inverse Leslie effect is also discussed.

## 1 Introduction

There are many examples in non-equilibrium thermodynamics of crossed effects that satisfy Onsager's reciprocity principle. Among classical examples one can cite the thermoelectric Peltier and Seebeck effects that are the basis of thermocouples and Peltier temperature controller. Less known is the Leslie thermomechanical effect found in cholesteric liquid crystals (twisted chiral nematic phases). In this case, a heat flux arising from a temperature gradient exerts a torque on the chiral molecules[1], which can be set into continuous rotation[2,3].

A chemical equivalent of the Leslie thermomechanical effect was predicted by de Gennes[4] and was evidenced for the first time by Tabe and Yokoyama in a Langmuir monolayer made of a chiral liquid crystal deposited on the free surface of water[5,6]. In that experiment, molecules covered the air/water interface, forming a monolayer with a long range orientational order. Molecules were tilted with respect to the normal to the surface, and their average in-plane orientation could be characterized by the $\vec{c}$-director (Fig. 1). Observations using Brewster angle microscopy (BAM)[7,8] revealed a continuous rotation of $\vec{c}$ when the monolayer was subjected to the evaporation of the water molecules from the subphase. In other words, the liquid crystal molecules act as a windmill driven by the flux of evaporating water. In practice the films are never uniform, and display characteristic Schlieren textures[9] containing singularities such as disclinations or walls. Because of these defects, the director field is strongly distorted and the molecules cannot rotate freely. Rotation is fastest in defect-free regions and is blocked by defects or impurities present in the film. This results in the formation of $2\pi$-walls, across which the director rotates by $2\pi$, that are organized as target patterns as seen under BAM observation (Fig. 2(c)). These patterns evolve constantly until accumulated elastic stress is strong enough to stop the molecular rotation in the central region.

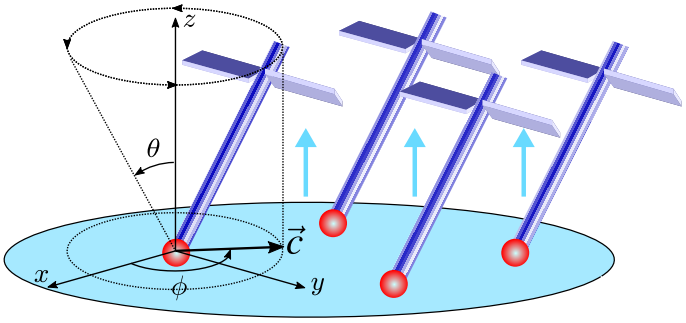


**Fig. 1** Schematic diagram of the organization of amphiphilic molecules at the air-water interface, and definition of the orientation angles and $\vec{c}$-director. The molecular azimuth $\phi$ changes with time because of the flux of water molecules (blue arrows in the diagram) interacting with the chiral center. Representation inspired by reference[5].

Although targets had been previously observed in Langmuir monolayers of chiral compounds[10–12], it was in the seminal work of Tabe and Yokoyama[5] that such patterns were first attributed to a molecular rotation driven by the evaporation of water in the subphase. This work prompted additional theoretical[13–17]

[a] Univ Lyon, Ens de Lyon, Univ Claude Bernard, CNRS, Laboratoire de Physique, F-69342 Lyon, France. E-mail: felix.bunel@ens-lyon.fr
[b] Departament de Ciència de Materials i Química Física, Universitat de Barcelona, Martí i Franquès 1, 08028, Barcelona, Catalonia, Spain.
[c] Institute of Nanoscience and Nanotechnology (IN2UB), Universitat de Barcelona, Barcelona, Catalonia, Spain.

† Electronic Supplementary Information (ESI) available: chemical formula of the various compounds tested, evidence of the electric field homogeneity, calculus of the chemical potential difference and short movies of the experiments. See DOI: 10.1039/cXsm00000x/

and experimental[18–20] studies that featured both evolving target patterns and spirals when the rotation started with defects of strength $+1$[17,18]. In their publication, Tabe and Yokoyama claimed to have observed the rotation in all of the 14 chiral compounds they tested. In later experiments, however, Nitoń and co-workers[19–21] reported that they could only find molecular rotation in two of the four tested amphiphilic compounds, in particular in those where the chiral center was away from the polar group in the molecules i.e., away from the water/air interface.

In spite of the multiple experimental and theoretical studies on the subject, a precise measurement of the Leslie effect has not yet been performed. Previous studies never measured the Leslie coefficient alone but only its ratio with the viscosity from the rotation speed of the molecules. Furthermore, these measurements were performed on target patterns for which the precession is slowed down by the accumulated stress, which can even stop the rotation when the elastic stress equilibrates the Leslie effect. Consequently, the speed of rotation depends on multiple parameters which are the Leslie coupling, the viscosity, the elastic constant, the target size, and the number of $2\pi$-walls within the target. As a result, it is hard to have a precise value for the Leslie coefficient from these measurements.

In this work we provide a full quantification of the Leslie effect by preparing large areas in the Langmuir monolayer where the $\vec{c}$-director is homogeneously aligned. In these domains the elastic effects can be neglected and the molecules rotate freely with a uniform angular velocity that only depends on the ratio of the Leslie coefficient over the rotational viscosity of the monolayer. We take advantage of the electric field we employ to prepare the homogeneous domain to perform additional experiments where we oppose the electric field driving with the Leslie effect, thus obtaining additional ratios between the Leslie coefficient and material parameters. Finally, we analyze the time correlations of the $\vec{c}$-director thermal fluctuations to measure the monolayer viscosity and elastic constant, allowing us to obtain an independent measure of the Leslie coefficient. This allows to estimate the potential efficiency of the inverse Leslie effect, which has been theorized[22]. However we demonstrate that its use as a microscale pump would be unpractical in this system.

The structure of the paper is as follows. In Sec. 2 we present the theoretical background that we employ to analyze the different dynamical scenarios put into evidence by the experiments. In Sec. 3, we describe the experimental setup, a characterization of the studied Langmuir monolayer, and a description of the experimental methods. The results are presented in Sec. 4 and discussed in Sec. 5. Finally, the conclusions are exposed in Sec. 6.

## 2 Theoretical background

The equation governing the dynamics of the $\vec{c}$-director can be derived with the help of the two Onsager relations that describe the coupled irreversible processes involved in the Leslie effect. The two coupled fluxes are the rotation rate of the $\vec{c}$-director, $\Omega$, and the evaporation rate of water across the monolayer, $J$. The two corresponding forces are the torque applied to the molecules, $\tau$, and the chemical potential difference of water molecules on either side of the monolayer, $\Delta\mu$. The constitutive relations read[5]:

$$\Omega = \frac{1}{\gamma}\tau + \frac{b}{\gamma}\Delta\mu, \tag{1}$$

$$J = \frac{b}{\gamma}\tau + P\Delta\mu. \tag{2}$$

Equation (1) describes the evolution of the orientation of the $\vec{c}$-director under the action of the Leslie force $\Delta\mu$ and the mechanical torque acting on the molecules. When $\tau = 0$, $\Delta\mu$ makes the director rotate continuously. This equation can be rewritten as a partial differential equation for the azimuthal angle $\phi$, which defines the $\vec{c}$-director (Fig. 1):

$$\gamma\frac{\partial\phi}{\partial t} = K\nabla^2\phi + P_s E\sin(\Phi_E - \phi) + b\Delta\mu. \tag{3}$$

In this equation, the monolayer is characterized by $\gamma$, the rotational viscosity, $K$, the elastic constant (assuming that bend and splay constants are equal), and $P_s > 0$, the spontaneous polarization. $E$ is the intensity of the in-plane electric field (oriented at an angle $\Phi_E$), and $b$ is the Leslie coefficient. Note that $\phi$ denotes here the angle between the polarization and the $x$-axis, which amounts to setting $\vec{c} = \vec{P}_s/P_s$. In general, $\vec{P}_s$ will not be exactly parallel to the optical axis of the molecules. As a result, this definition of the $\vec{c}$-director implies an unknown offset in $\phi$ with respect to the definition in Fig. 1. However, only changes in $\phi$ will be important in the phenomena described herein, which makes this offset physically irrelevant and, thus, can be ignored.

Equation (2) describes how the evaporation rate changes due to the presence of the two forces. The constant $P$ is the water permeability of the monolayer. At saturated water vapor pressure, $\Delta\mu = 0$, and the water flux can be expressed as

$$J = b\frac{\partial\phi}{\partial t}, \tag{4}$$

which is the inverse Leslie effect.

Experimentally, we can control $E$ and $\Phi_E$ with the electrodes placed in the trough (Sec. 3.2), and $\Delta\mu$ by adjusting the relative humidity $R_H$ above the surface according to the relation $\Delta\mu = RT\ln(R_H) \leq 0$, where $R$ is the gas constant and $T$ the absolute temperature[†].

The different terms in eqn (3) can be isolated by suitable experimental conditions. This way, ratios between all material parameters may be experimentally measured.

## 3 Materials and methods

### 3.1 Materials

We studied Langmuir monolayers of the ferroelectric liquid crystal (S)-4-[4-(1-methylheptyloxycarbonyl)phenyl]-4'-[6-(propanoyloxy) hexyloxy] biphenyl-4-carboxylate (Fig. 2(a)). Its bulk phase sequence is Crystal – 54.1°C – Smectic-C* – 74.4°C – Smectic-A – 95.8°C – Isotropic. The Langmuir isotherms of this compound were reported earlier[19] and were successfully reproduced with our experimental setup (Fig. 2(b)). Target patterns and Leslie rotation were observed at room temperature in the pressure range 0.5 mN.m$^{-1}$ until 15.0 mN.m$^{-1}$, where the mono-

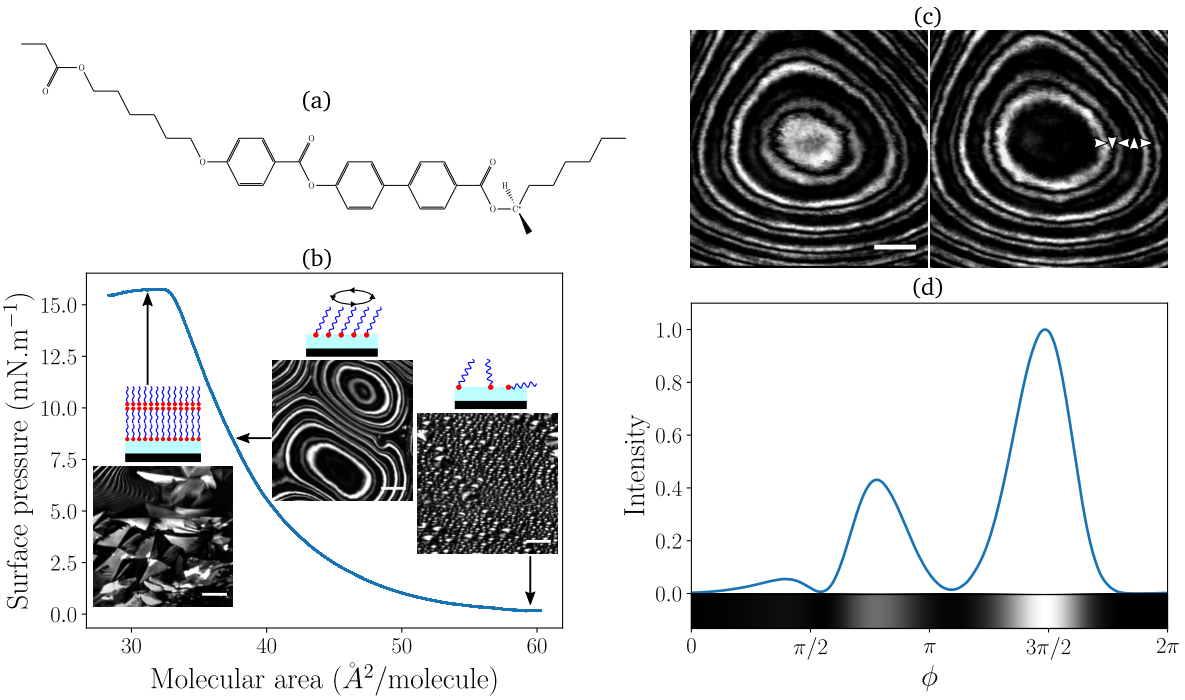


**Fig. 2** (a) Chemical structure of the ferroelectric chiral liquid crystal used in our experiment. (b) Surface pressure as a function of the molecular area during compression. (c) Brewster angle microscopy image of a Langmuir monolayer of the chiral compound. The two images are snapshots from an available video separated by 25 s. The rings are expanding and the intensity in the middle oscillates with a period of 50 s. The small arrows in the second image represent the $\vec{c}$-director, which rotates by $2\pi$ between two bright white rings. (d) Reflected intensity as a function of the azimuthal angle of the molecules. The polarizers were uncrossed by 3° so that $I(\phi) \neq I(-\phi)$. From the comparison of (c) and (d) we can determine that the molecules rotate in the counter clockwise direction. All scale bars are 0.1 mm.

layer collapsed into rigid multilayers. Although not presented in this work, we also observed the Leslie rotation for several other chiral liquid crystal compounds, whose formulas are given in the supplementary material[†]. It is worth mentioning that we tested in particular the two compounds of Nitoń and co-workers that were found not to rotate at room temperature[19,21]. However, we were able to observe the ordered phase and the Leslie rotation by heating the subphase above 40°C. This suggests that a regime with Leslie rotation can be achieved with a wide array of compounds, regardless of the position of the chiral center within the molecule.

### 3.2 Experimental setup

All our experiments were performed inside a custom-built Teflon trough of size $240 \times 76 \times 3$ mm$^3$. The subphase was ultrapure water supplied by a Milli-Q water purification system. The temperature of the subphase was maintained at $25 \pm 0.2$°C using a cooling/heating circulating bath and monitored with a thermocouple placed inside the water. The trough was placed inside a 1 m$^3$ enclosure to minimize thermal and air drifts. The relative humidity above the water was increased using a room humidifier (60065UHW, Medisana) and decreased with a flux of dry nitrogen and a vacuum pump. The relative humidity was recorded using a hygrometer (HH311, Omega Engineering) with a remote probe placed just above the water surface.

The monolayers were spread at the air-water interface from a 1 mg.mL$^{-1}$ solution prepared by dissolving the liquid crystal compound in chloroform (p.a. grade, Baker 7386). After spreading the solution, we waited at least 5 minutes to allow the solvent to evaporate and the monolayer to reach equilibrium. The surface area of the monolayer was adjusted by symmetrically moving two motorized Teflon barriers. The barriers were closed at a speed of 0.05 mm.s$^{-1}$ which corresponded to a compression rate of about 1 Å$^2$.molecule$^{-1}$.min$^{-1}$. The surface pressure of the monolayer was monitored using a filter paper Wilhelmy plate attached to a balance (R&K), calibrated before each experiment. The system is computer controlled with a custom LabView program. Unless otherwise stated, all measurements reported below were carried out at a surface pressure of 8 mN.m$^{-1}$ which was maintained constant by using a feedback loop in the control software.

The electric field was applied to the monolayer with four $1.8 \times 0.5 \times 0.5$ cm$^3$ parallelipedic electrodes. The electrodes were made of copper and were plated in Ni to minimize corrosion. They were immersed in the water less than 1 mm below the surface. Each of the electrodes was connected to an analogue output

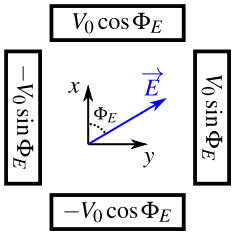


**Fig. 3** Configuration of the electrodes used in the experiment.

of a NI-6299 USB device (National Instruments). The four tension generators were internally connected to a common ground. To control both the intensity and the direction of the field, the four electrodes were fixed in a square insulated frame of size $d = 2\,\mathrm{cm}$ and supplied with appropriate voltages given in Fig. 3.

We computed the resulting electric field in this geometry with Mathematica and found that it forms an homogeneous in-plane field of intensity $E = 0.85 \cdot 2V_0/d$ and orientation $\Phi_E$ in the $0.4 \times 0.4$ cm$^2$ region in the center of the electrodes[†]. All the experiments were performed within this region where the field is uniform.

### 3.3 Brewster angle microscope

Imaging of the monolayer was performed with a custom-built depolarized Brewster angle microscope[7,8]. The intensity observed with the microscope depends on the local orientation of the molecules given by the molecular tilt $\theta$ and the azimuthal angle $\phi$[23,24] (Fig. 1). Since our experiments were performed at a fixed pressure, we considered that $\theta$, which varies with the surface pressure[24,25], remained constant and that the reflected intensity $I$ only depended on $\phi$. Note that $\theta$ can also change to reduce the stress in the regions strongly distorted with a large gradient of $\phi$[26]. In our experiments, this only happened near the core of the defects. As all of our measurements were done far from the defects, we systematically neglected this effect.

Imaging was performed with an analogue IR-enhanced CCD camera (JAI-CV-M50IR). The signal was subsequently digitized for storage and further computer processing. For fluctuation measurements, images were captured with an sCMOS camera (Zyla 4.2MP, Andor).

The calibration curve $I(\phi)$ was obtained by measuring the BAM reflected intensity in a well oriented domain submitted to a rotating electric field. In these conditions, the molecules align along the field at all time ($\phi \approx \Phi_E$) and $I(\phi)$ is obtained by directly recording the intensity as a function of time. An example of calibration curve is shown in Fig. 2(d). We performed this measurement for different values of the field (ranging between 1 and 6 V.cm$^{-1}$) and did not observe any change in the reflected intensity, indicating that $\theta$ is not altered by the electric field.

Although this calibration is easily reproducible, it strongly depends on the Brewster angle microscope settings (incidence angle, p-polarized light, and analyzer orientation). For this reason, a new calibration was performed at the beginning of each experiment. This way, it was possible to accurately determine the orientation of the molecules from the intensity measurements.

### 3.4 Preparation of large monodomains

As explained above, a clear observation of the Leslie rotation demands large monodomains with a uniform orientation of the molecules. In the case of large regions with a stripe patter of $2\pi$-walls (Fig. 4a), which occupied most of the monolayer, we devised a protocol that combined the use of a humidifier and an in-plane electric field to achieve these domains. The mist emitted by the humidifier resulted in water micro-droplets that sedimented on the air/water interface. This often led to the nucleation of pairs of complementary point defects on the $2\pi$-walls (Fig. 4b). We found that imposing a square-wave AC field of 2Hz and 2V.cm$^{-1}$ could also nucleate the defects. Once created, the $2\pi$-walls attached to the defects spontaneously shorten: the two defects move away from each other to relieve the wall stress[†], as predicted by Tsori and de Gennes[16]. This unwrapping was accelerated by imposing a DC electric field, which also helped to prevent the formation of new rotations during the annihilation of the defects (Fig. 4c,d). Note that application of a DC electric field alone, without the concurrent nucleation of defects, did not unwind the $2\pi$-walls. It only compressed them to maximize the surface area of the regions in which the molecules align along the field (Sec. 4.5).

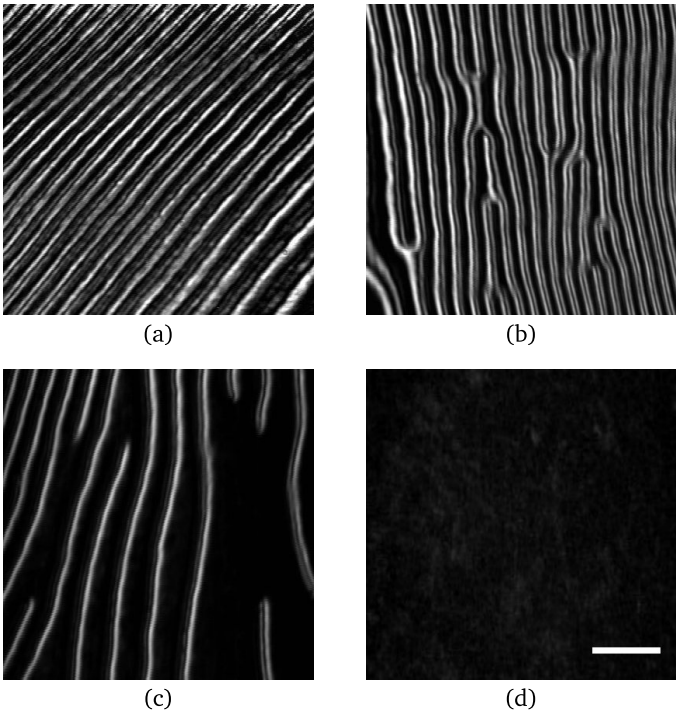


**Fig. 4** Brewster angle microscopy images of a Langmuir monolayer summarizing the process to obtain a large area of uniform orientation. (a) Initially, the monolayer is populated with $2\pi$-walls due to the Leslie rotation. (b) Defects are nucleated with the aid of the humidifier. (c) Upon application of an electric field, the defects move away from each other resulting in uniform domains. (d) After 5 minutes, all the walls have been eliminated. The scale bar is 0.1 mm.

In the case of either target patterns or spiral arms organized by a $\pm 1$ defect, an other efficient method to obtain a uniform area was to apply a DC electric field and rotate in the direction opposite to the Leslie rotation. This led to the progressive disappearance of the $2\pi$-walls, leaving an area with uniform molecular orientation.

Using the above protocols, we were able to obtain uniform domains that were 2 to 10 times larger than the field of view of the microscope, which was about 1 mm$^2$. This is 10 to 50 times larger than the area of the target patterns previously achieved in the literature.[5,19–21]. It is important to note that a free rotation of the molecules can only be observed on domains at least this wide. Elastic effects can indeed be neglected when $K\nabla^2\phi \ll b\Delta\mu$

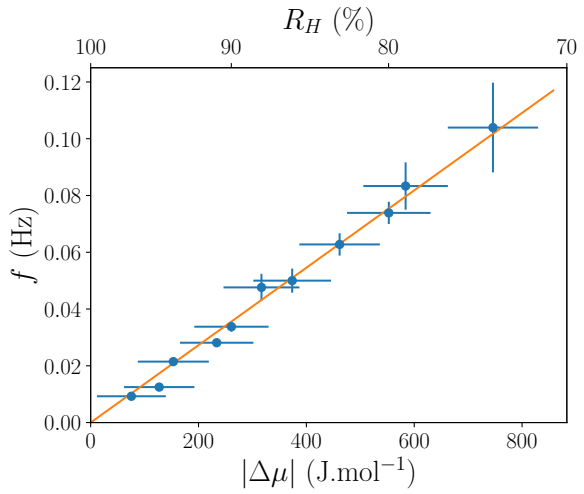


**Fig. 5** Frequency of rotation as a function of the chemical potential difference applied to an unconstrained monolayer. The solid line is a linear fit to the data.

so only when the size of the oriented domain is much larger than $K/b\Delta\mu \sim 0.5$ mm$^2$ (calculated with the value of $b/K$ given in Sec 4.2).

# 4 Results

## 4.1 Unconstrained Leslie rotation

Once a large area of uniform orientation was created, we switched off the electric field to release the rotation of the molecules. In the absence of constraints, molecules rotate without being slowed down by elasticity[†]. As a consequence, eqn (3) now results in:

$$\gamma\frac{d\phi}{dt} = b\Delta\mu. \tag{5}$$

Solving this equation gives $\phi = 2\pi ft$ with:

$$f = \frac{b\Delta\mu}{2\pi\gamma} \tag{6}$$

By recording the BAM intensity as a function of time and by using the calibration curve $I(\phi)$, we determined that molecules were rotating in the counterclockwise direction ($f > 0$). This allowed us to determine that $b$ is negative, since $\Delta\mu$ is negative and $\gamma$ must be positive. Experiments at different relative humidity allowed us to verify that $f$ is proportional to $\Delta\mu$ (Fig. 5) in agreement with eqn (6). Data analysis yielded the value of the ratio between the Leslie coefficient and the viscosity,

$$\frac{b}{\gamma} = -8.6 \pm 0.8 \;\; 10^{-4} \text{ mol.J}^{-1}\text{.s}^{-1}.$$

In these experiments, we observed that the rotation frequency could be as high as 0.1 Hz. This value is larger than those reported by Tabe and Yokoyama at an even lower relative humidity of 50% (*i.e.* higher Leslie torque)[5]. This is likely due to the fact that we used a pure chiral compound, whereas Tabe *et al.* used a mixture composed of 90% of an achiral compound and 10% of a chiral dopant. We can also compare our results to the ones obtained by Milczarczyk-Piwowarczyk *et al.* with the same compound used here[19,21]. At a relative humidity of 65%, they reported a frequency of 0.07 Hz, which is half the one found by extrapolating our data. This difference can be attributed to the fact that their measurements were done in the center of relatively small target patterns in which the rotation was slowed down by the elasticity of the monolayer.

## 4.2 Target patterns at equilibrium

Even though the unconstrained Leslie rotation is possible only in the absence of disclinations and walls, it is interesting to study small constrained regions that develop equilibrium target patterns, in which molecular rotation has stopped because of a balance between the Leslie and the elastic torques. In this limit, eqn (3) becomes

$$0 = K\nabla^2\phi + b\Delta\mu\,. \tag{7}$$

Experimentally, the small constrained regions are formed by impurities or remains of the isotropic phase. We observe that the equilibrium pattern depends mostly on two parameters –the size of the pattern and the relative humidity. The dependency on the size of the pattern is simple: if the surface area is large, more $2\pi$-walls must be created to stop the rotation. The influence of the humidity can be seen by comparing the photographs of the same target pattern taken after equilibration at two different relative humidities (Fig. 6(a) and 6(b)). As expected, the number of $2\pi$-walls and the elastic stresses increase when the humidity decreases because the Leslie torque increases.

These dependencies can be explained by transforming eqn (7)

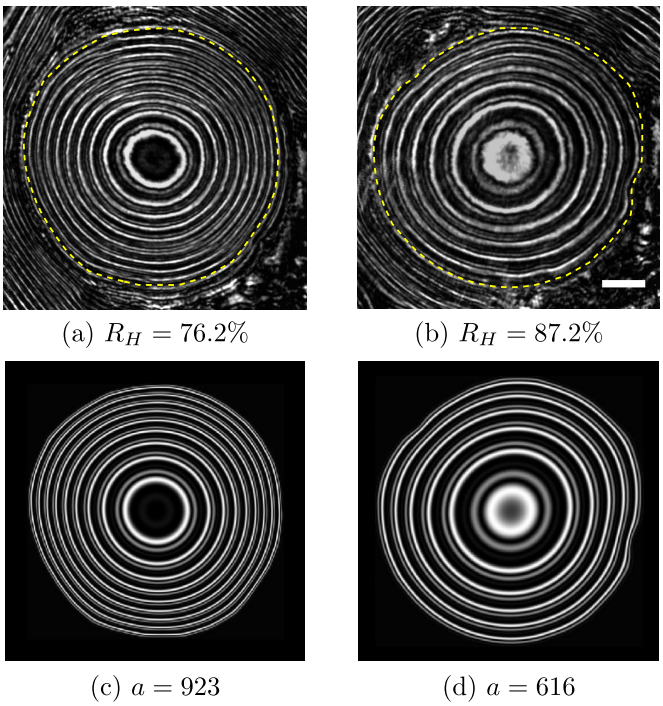


**Fig. 6** Experimental (a and b) and simulated (c and d) equilibrium target patterns. The target pattern is the same on the two experimental images and only the humidity changed. The shape of the boundary of the experimental pattern is used for the simulation. The scale bar is 0.1 mm.

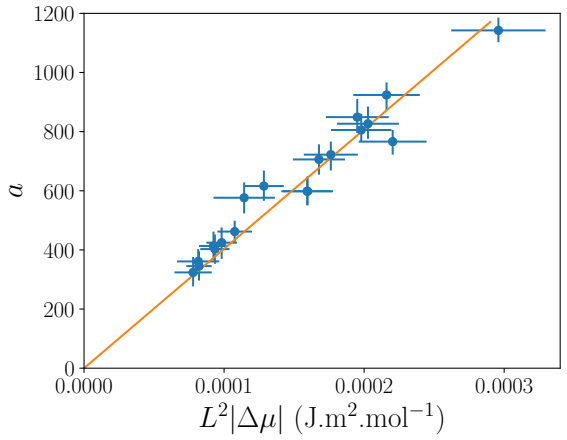


**Fig. 7** Calculated parameter $a$ as a function of a scaling parameter that takes into account the size of the pattern and the chemical potential difference applied to the monolayer. The error bars in $a$ are obtained by determining the value that gives plus or minus half a rotation at the center in comparison to the one that best reproduces the target pattern. The solid line is a linear fit to the data.

into a dimensionless form:

$$0 = \tilde{\nabla}^2\phi + a. \tag{8}$$

Here, we have rescaled the distances by the size of the observed domain, $L$, so that $\tilde{\nabla}^2 = \nabla^2/L^2$. With these units, the equilibrium target pattern depends on a single dimensionless parameter,

$$a = \frac{bL^2\Delta\mu}{K}. \tag{9}$$

The smaller this parameter, the more important the effect of the elasticity is and the less rotations are necessary to reach equilibrium. More precisely, the number of $2\pi$-walls in the stationary state is proportional to $a$. The dependency of $a$ on the size of the pattern and the relative humidity (through $\Delta\mu$) is in agreement with the experimental observations described before. Equation (8) can be solved analytically as a series of Bessel functions in the case of circular boundary conditions [18], or numerically for any kind of boundary shape [17,18].

The equilibrium target patterns can be analyzed by comparing the experimental images with the numerical simulations. A quantitative comparison can be performed by using the same boundary conditions in the simulations as in the experiments. Under the assumption that the anchoring at the boundary is of infinite strength, we can solve eqn (8) for different values of $a$ and find the one that best reproduces the experimental image. As it can be seen in Figure 6, the agreement between the experiment and the simulations is excellent considering that the simulation depends on the single parameter $a$. A more accurate reproduction of the target pattern can be achieved by adding some noise to the simulation [17].

In Figure 7, we have plotted as a function of $L^2|\Delta\mu|$ the value of $a$ obtained by comparing the simulated target patterns with the experimental ones observed at equilibrium. In this graph, the points correspond to target patterns of different sizes and obtained with different relative humidities. As predicted by eqn (9), $a$ is a linear function of $L^2|\Delta\mu|$ within the experimental errors. From the slope of this curve, we deduced a new ratio:

$$\frac{b}{K} = -4.1 \pm 0.3\ 10^6\ \text{mol.m}^{-2}.\text{J}^{-1}.$$

### 4.3 Rotational diffusivity and elastic constant from thermal fluctuations

Experiments presented so far are based on the competition between Leslie rotation and the viscous or the elastic torques in the liquid crystal monolayer. These analyses yield ratios between $b$ and the material parameters $\gamma$ and $K$. In order to obtain $b$, we need to rely on independent measurements to measure these material parameters. To this purpose, we have resorted to an analysis of the thermal orientational fluctuations of the $\vec{c}$-director on a well oriented area. The mean square difference $\sigma^2(t) = \langle|\phi(0) - \phi(t)|^2\rangle$ is expected to diverge logarithmically with time as [27,28]:

$$\sigma^2(t) = \frac{k_B T}{2\pi K} \ln\left(1 + \frac{Kt}{\gamma\alpha}\right). \tag{10}$$

Here, $\alpha$ is the surface area over which average instantaneous intensities are measured. This study requires that the director has no collective rotation or drift. We blocked the Leslie rotation by working at high humidities under a weak electric field of $E = 0.25$ V.cm$^{-1}$. It must be emphasized that the electric field does not influence the form of eqn (10) on the condition that $\alpha$ is small in comparison to $\lambda^2$, where $\lambda = \sqrt{K/P_s E}$ is the electric coherence length (the field only dampens the fluctuations of wavelength larger than $\lambda$ [29]. This condition was always satisfied in our experiments, where $\alpha = 1\,\mu\text{m}^2$ and $E = 0.25$ V.cm$^{-1}$. With the value of $K/P_s$ measured in Sec 4.5, this gives $\lambda \approx 30\,\mu$m and $\alpha/\lambda^2 = 0.003$, which is indeed much smaller than 1. Instantaneous molecular orientations were computed from the recorded average BAM intensity according to the calibration curve, and were numerically processed to obtain $\sigma^2(t)$. Fig. 8 shows measurements of $\sigma^2(t)$ performed in different regions of the monolayer. Each curve has

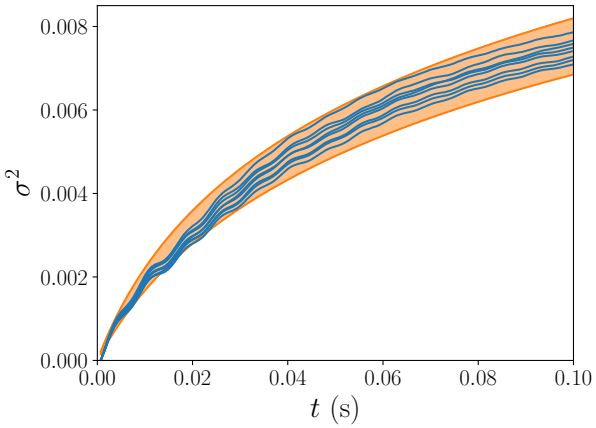


**Fig. 8** Mean square difference in molecular orientation as a function of time. The different curves corresponds to different experiments. The colored area correspond to the results of eqn (10) with the values for $K$ and $K/\gamma$ taken within the error bars specified in the text.

been averaged over at least 5000 measurements of 0.1 s of total duration, with a sampling rate of 1400 Hz. We observe that the mean square difference in orientation is consistent with the expected logarithmic behavior. The observed small oscillations, which were also detected in the absence of a monolayer, are due to an artifact coming from the imaging system, and do not affect the overall trend of the data. By fitting the data of Fig. 8 with eqn (10) we obtained:

$$\frac{K}{\gamma} = 1.7 \pm 0.2\ 10^{-10}\ \mathrm{m}^2.\mathrm{s}^{-1} \qquad \text{and} \qquad K = 1.8 \pm 0.1\ 10^{-19}\mathrm{J}.$$

This estimation for $K/\gamma$ can be checked by measuring the velocity of two defects of opposed sign moving away from each other in the middle of the $2\pi$-walls, a situation visible in Fig. 4(b) and in a video available as supplementary material. This velocity was theoretically calculated by Tsori and De Gennes [16]:

$$v = 2\frac{K}{\gamma}\left(|\nabla\phi_0| - \frac{1}{2R}\right) / \ln\left(\frac{L}{a}\right). \tag{11}$$

Here, $|\nabla\phi_0|$ is the local gradient of orientation of the molecules when there is no defect, $R$ is the distance between the two defects, $L$ is the size of domain in which the deformation relaxes and $a$ is the core radius of the disclination, which is typically of the order of the molecular size $\sim 3.5$ nm. This speed was measured experimentally when the two defects were far away from each other, i.e. $1/2R \sim 0$, and the speed was constant with time, and was found to be of the order of 0.2 mm/min. BAM images allowed us to determine the local gradient $|\nabla\phi_0| \sim 4\pi/0.1$ mm and the size of the domain $L \sim 1$ mm. In consequence, eqn (11) gives us a value for the ratio $K/\gamma$ that is of the order of $2\ 10^{-10}\ \mathrm{m}^2.\mathrm{s}^{-1}$, in correct agreement with the previous value found from the analysis of the fluctuations.

### 4.4 Coupling Leslie rotation with an electric field

Although the above measurements are sufficient to measure the Leslie coefficient, the ability to apply an arbitrary in-plane electric field allows to obtain ratios between the material parameters $b$, $K$, and $\gamma$ with the monolayer spontaneous polarization, $P_S$. By doing this we can decrease by 50% the error bar on our estimate for $b$, as discussed below.

First, we analyze the dynamics of large uniform areas of the monolayer in the presence both of the Leslie and the electric field torques. For this, we must refer to the equation governing the dynamics of $\phi$,

$$\gamma\frac{d\phi}{dt} = P_s E \sin(\Phi_E - \phi) + b\Delta\mu. \tag{12}$$

This equation predicts the existence of two regimes.

At large electric fields ($E > E_c = b\Delta\mu/P_s$), there is an angle $\phi_{eq}$ at which $P_s E \sin(\Phi_E - \phi_{eq}) + b\Delta\mu = 0$ and the rotation stops. For $E = E_c$, the equilibrium $\vec{c}$-director is perpendicular to the electric field

At small electric fields ($E < E_c$), the electric torque is always smaller than the Leslie torque and the molecules keep rotating due to water evaporation.

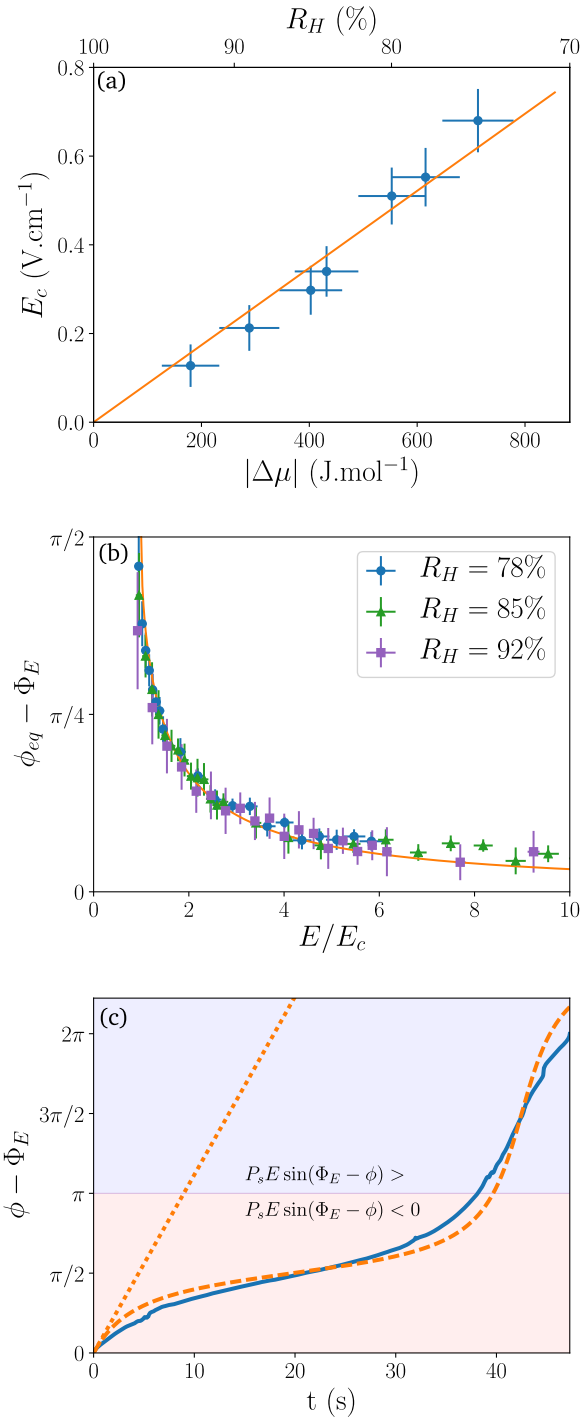


**Fig. 9** (a) Critical electric field for the onset of rotation as a function of the chemical potential difference applied to the monolayer. The continuous line is a linear fit to the data. (b) Equilibrium molecular alignment offset as a function of the scaled electric field strength in the equilibrium regime (above $E_c$). The continuous line corresponds to the prediction of eqn (13) without any adjustable parameters. (c) Angle with the applied electric field in the rotating regime (below $E_c$). The measurement was performed at $R_h = 84\%$ and $E = 0.34$ V.cm$^{-1}$. The solid line corresponds to the data. The dashed line has been obtained from eqn (14) with the values of $r$ and $f$ calculated from the experimental values of $b/P_s$ and $b/\gamma$. The dotted line corresponds to the case $E = 0$ at the same relative humidity.

Experimentally, $E_c$ was obtained by slowly decreasing E from values at which the rotation was blocked. The results for different humidities are shown in Fig. 9(a), where the predicted dependence of $E_c$ on $\Delta\mu$ is verified.

From the slope of this curve we deduced the ratio:

$$\frac{b}{P_s} = -8.2 \pm 0.9\ 10^{-2}\ \text{mol.m}^{-1}.\text{C}^{-1},$$

with a explicit minus sign since $b$ is negative and $P_s$ is positive by convention.

We also measured the equilibrium angle $\phi_{eq} - \Phi_E$ between the molecules and the field at large electric fields when the rotation was blocked. According to eqn (12), this angle reads

$$\phi_{eq} - \Phi_E = \sin^{-1}\left(\frac{b\Delta\mu}{P_s E}\right) = \sin^{-1}\left(\frac{E_c}{E}\right). \qquad (13)$$

The corresponding measurements are shown in Fig. 9(b) for different values of the field and the humidity. The data is in good agreement with eqn (13), as all measurements collapse on the same master curve when $E$ is scaled with $E_c$.

Below the critical field, the molecules rotate continuously but their angular velocity changes over time. They are slowed by the field when $0 < \phi - \Phi_E < \pi$ and accelerated when $\pi < \phi - \Phi_E < 2\pi$. The variations of $\phi$ can be calculated by solving eqn (12) when $E < E_c$, resulting in

$$\phi(t) - \Phi_E = 2\tan^{-1}\left(r + \sqrt{1-r^2}\tan\left(\sqrt{1-r^2}\pi f t + C\right)\right). \qquad (14)$$

Here, $r = E/E_c$, $f$ is the intrinsic frequency given by eqn (6), and $C$ is a constant of integration.

The predictions of eqn (14) are in correct agreement with the experimental measurements (see Fig. 9(c) for the comparison). Some deviations from the theoretical curve are nonetheless visible. They are probably due to the fact that we neglected the elasticity in this experiment. Indeed, images revealed that the rotation was not perfectly uniform across the domain, which is the hallmark of elastic effects. In addition, we noted that these measurements were extremely sensitive to the variations of humidity, the two parameters $r$ and $f$ used in eqn (14) strongly depending on $R_h$ via $\Delta\mu$. This makes this experiment difficult to control.

### 4.5 Compression of a $2\pi$-wall under electric field

To conclude the account of results, we present experiments that enable to determine the ratios $K/P_s$ (this section) and $\gamma/P_s$ (next section), which will be used to improve the precision of our measurement of $b$. The ratio $K/P_s$ was determined by observing the compression of an isolated $2\pi$-wall in the presence of an electric field (see Fig. 10(a)).

At high humidity ($\Delta\mu = 0$), the width at equilibrium of a wall results from a competition between the elastic and electric torques. For a straight wall along the $y$-axis, $\phi$ is only function of $x$, and the general torque equation simplifies to

$$\frac{d^2\phi}{dx^2} = -\frac{P_s E}{K}\sin(\Phi_E - \phi). \qquad (15)$$

The solution to this equation with the boundary conditions

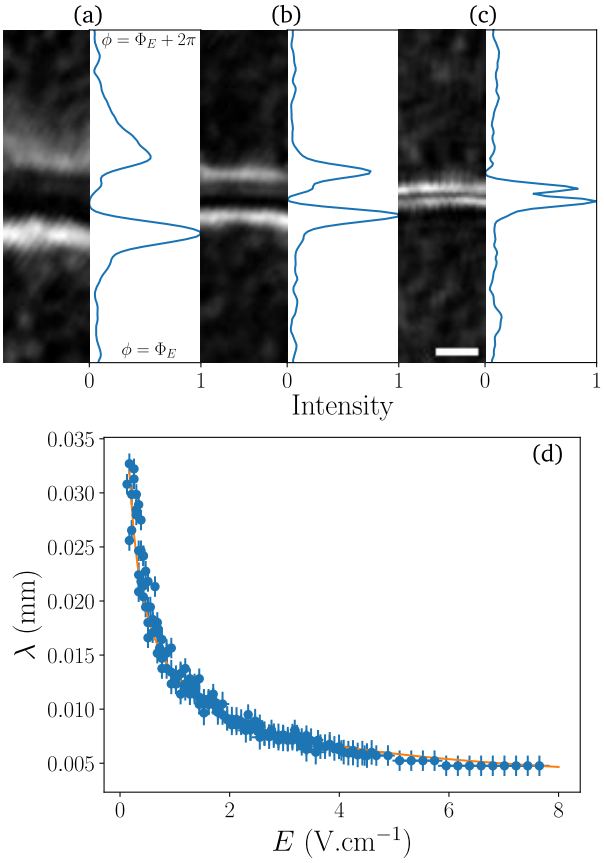


**Fig. 10** (a)(b)(c) BAM micrographs and normalized intensity profiles of an isolated $2\pi$-wall under different electric field intensities.(a) $E = 0.8$ V.cm$^{-1}$; (b) $E = 2.3$ V.cm$^{-1}$; (c) $E = 13.6$ V.cm$^{-1}$. The direction of the field was set at $\Phi_E = 200°$, which corresponds to the minimum of intensity between the two bright fringes in Figure 2(d). The scale bar is 0.03 mm. (d) Characteristic length $\lambda$ as a function of the electric field applied to the monolayer. The continuous line is a fit to the data with $\lambda \propto 1/\sqrt{E}$. The scale bar is 0.03 mm.

$\phi(-\infty) = \Phi_E$ and $\phi(+\infty) = \Phi_E + 2\pi$ is:

$$\phi(x) - \Phi_E = 4\tan^{-1}(e^{x/\lambda}), \qquad (16)$$

where

$$\lambda = \sqrt{\frac{K}{P_s E}} \qquad (17)$$

is a characteristic length-scale that sets the width of the wall.

Experimentally, we chose $2\pi$-walls that were at least 0.2 mm apart from others. This was essential to satisfy the boundary conditions assumed above. In practice the intensity profiles were too noisy to precisely calculate the profile $\phi(x)$ from the optical calibration curve. For this reason, we simplified the procedure by just measuring the distance between the two bright fringes of the intensity profile. From the calibration curve $I(\phi)$ (Fig. 2(d)) we know that these two fringes occur for particular values of $\phi$. This allows to measure $\lambda$ by analyzing these two $\phi(x)$ data points with the theoretical profile given in eqn (16).

The results of this study are shown in Fig. 10(b). The predicted

dependence $\lambda \propto 1/\sqrt{E}$ is confirmed, yielding the ratio

$$\frac{K}{P_s} = 1.7 \pm 0.3\ 10^{-8}\ \text{m.J.C}^{-1}\,.$$

### 4.6 Switching time after the application of an electric field

Finally, we can determine $P_s/\gamma$ from the analysis of the $\vec{c}$-director dynamics when it aligns with an electric field that is suddenly applied[29]. For convenience, this measurement was performed in large well-oriented monodomains and at saturated vapor pressure. In these conditions, the elastic and Leslie torques can be neglected in eqn (3), which becomes:

$$\gamma \frac{d\phi}{dt} = P_s E \sin(\Phi_E - \phi) \tag{18}$$

Suppose that $\phi = \phi_0$ in equilibrium and that, at $t = 0$, an electric field of amplitude $E \neq 0$ with an orientation $\Phi_E$ is applied. The evolution of $\phi$ is obtained by solving eqn (18), and reads

$$\phi(t) - \Phi_E = 2\tan^{-1}\left(\tan\left(\frac{\phi_0 - \Phi_E}{2}\right) e^{-\frac{t}{\tau}}\right), \tag{19}$$

where

$$\tau = \frac{\gamma}{P_s E}\,. \tag{20}$$

is the characteristic switching time.

We performed this experiment for different values of $\phi_0 - \Phi_E$ and $E$. By recording the BAM intensity as a function of time and by using the calibration curve for the intensity, we determined $\phi(t)$. An example is shown in Fig. 11(a), where $\phi_0 - \Phi_E = \pi$. In all the cases, the curves were well fitted by eqn (19). This allowed us to measure $\tau$ as a function of $E$ (Fig. 11(b)) and to obtain the ratio

$$\frac{\gamma}{P_s} = 1.04 \pm 0.09\ 10^2\ \text{V.m}^{-1}\text{.s}.$$

This value may seem relatively high in comparison to similar values given in the literature. For instance, Tabe *et al.*[29] gave values ten times smaller. Below, we show that this is due to the large value of the viscosity $\gamma$, an expected result in view of the large surface pressure used in our experiments[27].

## 5 Discussion of the results

We have measured independently six ratios $b/\gamma$, $b/K$, $K/\gamma$, $b/P_s$, $K/P_s$ and $\gamma/P_s$ involving the four material constants, i.e. the Leslie coefficient $b$, the viscosity $\gamma$, the elastic constant $K$ and the horizontal component of the polarization $Ps$. In reality, these ratios are not independent because, for instance, $b/\gamma = (b/P_s)/(\gamma/P_s)$. Taking into account these relations, it is possible to increase the precision of our results. This was done by maximizing the global likelihood function of the problem that takes into account all the measurements and all the links between them[30]. This global

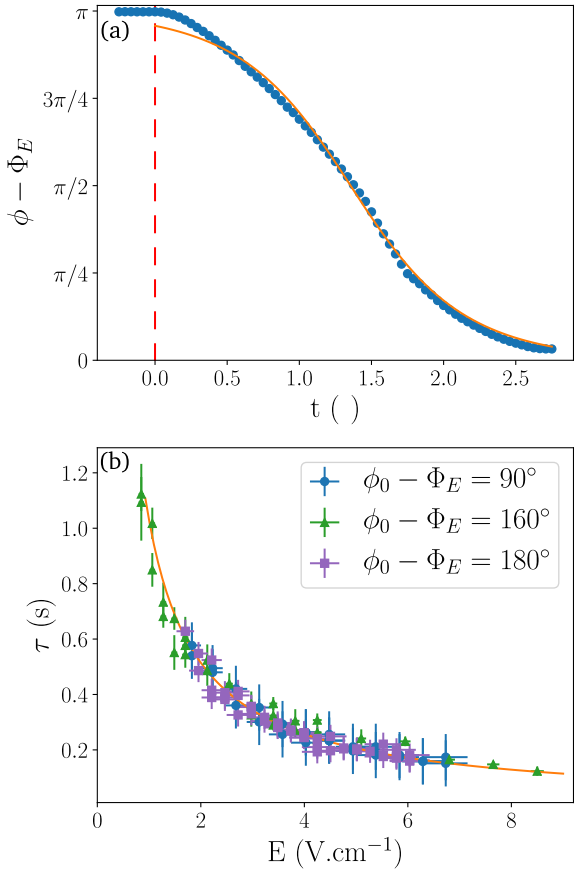


**Fig. 11** (a) Alignment dynamics upon application of an electric field of amplitude $E = 1.9$ V.cm$^{-1}$ at $t = 0$. The solid line corresponds to a fit of the data to eqn (19), which yields $\tau = 0.5$ s. (b) Response time $\tau$ as a function of the electric field. The solid line corresponds to a fit to the data with $\tau \propto 1/E$.

analysis led to the following values for the ratios:

$$\frac{b}{\gamma} = -7.8 \pm 0.5\ \ 10^{-4}\ \text{mol.J}^{-1}\text{.s}^{-1}$$

$$\frac{b}{P_s} = -8.0 \pm 0.4\ 10^{-2}\ \text{mol.m}^{-1}\text{.C}^{-1}$$

$$\frac{b}{K} = -4.3 \pm 0.3\ 10^{6}\ \text{mol.m}^{-2}\text{.J}^{-1}$$

$$\frac{K}{P_s} = 1.8 \pm 0.1\ 10^{-8}\ \text{m.J.C}^{-1}$$

$$\frac{\gamma}{P_s} = 1.00 \pm 0.08\ 10^{2}\ \text{V.m}^{-1}\text{.s}$$

$$\frac{K}{\gamma} = 1.8 \pm 0.1\ 10^{-10}\ \text{m}^2\text{.s}^{-1}$$

As a consistency check of this analysis, we computed the following three combinations of parameters that must be equal to 1 by construction:

$$\frac{b}{\gamma}\frac{\gamma}{P_s}\frac{P_s}{b} = 0.97 \pm 0.19 \qquad \frac{b}{K}\frac{K}{P_s}\frac{P_s}{b} = 0.97 \pm 0.19$$

$$\frac{b}{K}\frac{K}{\gamma}\frac{\gamma}{b} = 1.03 \pm 0.20$$

As we can see, these three combinations are equal to 1 within the experimental errors, confirming the consistency of our measurements.

From the values found for the ratios and the elastic constant $K$, we can calculate the other material parameters. This gives:

$$\begin{aligned} K &= 1.8 \pm 0.1\ 10^{-19}\ \text{J} \\ P_s &= 1.0 \pm 0.1\ 10^{-11}\ \text{C.m}^{-1} \\ \gamma &= 1.1 \pm 0.2\ 10^{-9}\ \text{kg.s}^{-1} \\ b &= -8 \pm 1\ 10^{-13}\ \text{mol.m}^{-2} \end{aligned}$$

We recall that these values were obtained at 25°C and for a surface pressure of 8 mN.N$^{-1}$. These measurements are consistent with the values reported in the literature. $K$ is usually of the order of $10^{-20}$ J in Langmuir monolayers but can vary from $10^{-18}$ to $10^{-21}$ J depending on the compound and the temperature[27,29]. Concerning the rotational viscosity, systematic measurements[27] showed that it increases with the surface pressure and decreases with the temperature and can vary over 3 decades from $10^{-11}$ to $10^{-9}$ kg.s$^{-1}$. Our fairly large value is certainly due to the fact that we worked at a relatively high surface pressure and at low temperature. Our value of $P_s$ seems a bit large in comparison with the one reported for monolayers of an azobenzene derivative, of order 2 $10^{-13}$ C.m$^{-1}$ [29]. Nevertheless, our measurements are consistent with estimations for the molecular dipole and can be justified by the microscopic-scale ordering of the molecules in the monolayer (See Appendix).

## 6 Concluding remarks

The chemical Leslie effect studied in this paper is due to the irreversible coupling between a chemical potential gradient and the rotation of chiral liquid crystals molecules. As such, it is very similar to the Peltier and Seebeck effects that couple a temperature gradient and an electric current. Similarly to a thermocouple that measures the temperature, the Leslie effect could be used, at least in principle, to measure humidity. The remarkably small deviation from a linear behavior (Fig. 5) suggests that the precision of the measurement could be even better than with usual capacitive hygrometers, in particular close to the saturation where the latter are very imprecise. Conversely, the inverse Leslie effect could be used as a microscopic pump just like a Peltier temperature controller creates a heat flux from an electric current. In our case, an active flux of water molecules could be induced by forcing the precession of the liquid crystal molecules, for instance by a rotating electric field. In this case, the limitations of the pump come from the maximum speed at which the electric field can rotate synchronously with the molecules. For our compound, this critical speed was found to be of the order of 10 revolutions per second for an electric field of 5 V.cm$^{-1}$. If we inject this rotation speed in eqn (4), we see that the maximum flux created by a Leslie effect-based pump is $J_{max} = b\,\omega_{max} \sim 10^{-14}$ mol.m$^{-2}$.s$^{-1}$. This flux is extremely small and corresponds to an evaporation rate of 2 $10^{-13}$ mL.m$^{-2}$.s$^{-1}$. In comparison, natural evaporation is 10 orders of magnitude larger with a rate of $10^{-2}$ mL.m$^{-2}$.s$^{-1}$ (as measured by placing a small Langmuir through on a Mettler Toledo XS 205 precision balance). This means that the efficiency of such a pump is quite limited and that the material transport caused by inverse Leslie effect is certainly impossible to measure experimentally. This conclusion should also apply to the free-standing films of ferroelectric Smectic C$^\star$ liquid crystals in which a similar chemical Leslie effect has been reported[31,32].

## Appendix

The macroscopic polarization $P_s$ can be derived from the microscopic polarization of the molecules, $P_1$, and the orientational correlation function[29]:

$$P_s \sim \frac{2}{2-x}\left(\frac{R}{\lambda}\right)^x P_1. \qquad (21)$$

Here, $\pi R^2$ is the area per molecule, an experimentally known quantity and $\lambda$ is the electric coherence length defined in eqn (17). The parameter $x$ characterizes the competition between the thermal fluctuations and the coherent behavior of the liquid crystal, and is given by $x = k_B T/2\pi K$. Since, in our case, $x$ is of the order of 4 $10^{-3}$, the spontaneous polarization $P_s$ is basically equal to $P_1$. The latter can be calculated from the molecular dipole $\mu$ and the area per molecule: $P_1 = \mu_\parallel/\pi R^2$. Here, it is important to note that only the horizontal component of the dipole $\mu_\parallel = \mu \sin(\theta)$ participates in the in-plane spontaneous polarization. The value of $\mu$ was obtained using DFT calculations (B3LYP functional and the TZVP basis set, as implemented in the Gaussian09 code), and was found to be around $\mu \sim 2.9$ D. As a result, $\mu/\pi R^2$ is of the order of 2.7 $10^{-11}$ C.m$^{-1}$. Having determined experimentally that $P_s = 1.0\ 10^{-11}$ C.m$^{-1}$, we calculate $\theta \sim 23°$. Finally, the computations show that the angle between the dipolar moment and the long axis of the molecule is 15°. We can thus conclude that the molecules are tilted from the normal to the interface by an angle ranging between 8° and 38°, depending on how the molecules organize in the monolayer.


## Acknowledgements

The authors thank Andrzej Żywociński for the compound used in this work and valuable discussions. The authors also thank Lubor Lejček for compounds used in preliminary experiments. The authors thank Jordi Ribas and Raúl Santiago (UB) for the calculation of the dipolar moment. This work was funded by MINECO Project FIS2016-78507-C2-1-P.


## Notes and references


1 F. M. Leslie, *Proc. Roy. Soc. A*, 1968, **307**, 359–372.
2 P. Oswald and A. Dequidt, *Europhys. Lett.*, 2008, **83**, 16005.
3 P. Oswald, *Europhys. Lett.*, 2014, **108**, 36001.
4 P. G. de Gennes, *The Physics of Liquid Crystals*, Clarendon Press, Oxford, 1973.
5 Y. Tabe and H. Yokoyama, *Nature Materials*, 2003, **2**, 806–

809.

6 *Although originally called Lehmann rotation, this phenomenon implies the existence of a chiral supramolecular arrangement. In the Leslie effect, the rotation is due to the existence of molecular-level chirality.*

7 S. Hénon and J. Meunier, *Review of Scientific Instruments*, 1991, **62**, 936–939.

8 D. Hoenig and D. Moebius, *The Journal of Physical Chemistry*, 1991, **95**, 4590–4592.

9 J. Nehring and A. Saupe, *J. Chem. Soc., Faraday Trans. 2*, 1972, **68**, 1–15.

10 J. Adams, W. Rettig, R. S. Duran, J. Naciri and R. Shashidhar, *The Journal of Physical Chemistry*, 1993, **97**, 2021–2026.

11 Y. Tabe and H. Yokoyama, *The Journal of Chemical Physics*, 2001, **115**, 1041–1051.

12 J.-L. Gallani, S. Mery, Y. Galerne and D. Guillon, *The Journal of Physical Chemistry B*, 2004, **108**, 11627–11632.

13 G. Watanabe, S. Ishizaki and Y. Tabe, in *Collective Precession of Chiral Liquid Crystals under Transmembrane Mass Flow*, World Scientific, 2012, pp. 138–146.

14 M. Yoneya, Y. Tabe and H. Yokoyama, *Ferroelectrics*, 2008, **365**, 139–147.

15 M. Yoneya, Y. Tabe and H. Yokoyama, *The Journal of Physical Chemistry B*, 2010, **114**, 8320–8326.

16 Y. Tsori and P.-G. d. Gennes, *The European Physical Journal E*, 2004, **14**, 91–96.

17 D. Svenšek, H. Pleiner and H. R. Brand, *Phys. Rev. Lett.*, 2006, **96**, 140601.

18 R. K. Gupta, K. A. Suresh, S. Kumar, L. M. Lopatina, R. L. B. Selinger and J. V. Selinger, *Phys. Rev. E*, 2008, **78**, 041703.

19 P. Milczarczyk-Piwowarczyk, A. Żywociński, K. Noworyta and R. Hołyst, *Langmuir*, 2008, **24**, 12354–12363.

20 P. Nitoń, A. Żywociński, M. Fiałkowski and R. Hołyst, *Nanoscale*, 2013, **5**, 9732–9738.

21 P. Nitoń, *PhD thesis*, IPCh PAS, Warsaw, 2012.

22 D. Svenšek, H. Pleiner and H. R. Brand, *Phys. Rev. E*, 2008, **78**, 021703.

23 Y. Tabe and H. Yokoyama, *Langmuir*, 1995, **11**, 699–704.

24 J. Ignés-Mullol, J. Claret and F. Sagués, *The Journal of Physical Chemistry B*, 2004, **108**, 612–619.

25 M. K. Durbin, A. Malik, A. G. Richter, C.-J. Yu, R. Eisenhower and P. Dutta, *Langmuir*, 1998, **14**, 899–903.

26 Y. Tabe, N. Shen, E. Mazur and H. Yokoyama, *Phys. Rev. Lett.*, 1999, **82**, 759–762.

27 A. Feder, Y. Tabe and E. Mazur, *Physical Review Letters*, 1997, **79**, 1682–1685.

28 D. H. Van Winkle and N. A. Clark, *Physical Review A*, 1988, **38**, 1573.

29 Y. Tabe, T. Yamamoto, I. Nishiyama, M. Yoneya and H. Yokoyama, *Japanese Journal of Applied Physics*, 2003, **42**, L406.

30 D. Taupin, *Probabilities, data reduction and error analysis in the physical sciences*, Ed. Physique, 1988.

31 K. Seki, K. Ueda, Y.-i. Okumura and Y. Tabe, *Journal of Physics: Condensed Matter*, 2011, **23**, 284114.

32 K. Seki, K. Ueda, K. Uda, K. Tsunekawa and Y. Tabe, *Japanese Journal of Applied Physics*, 2011, **50**, 125804.